

Article

# TiO<sub>2</sub> Catalyzed Dihydroxyacetone (DHA) Conversion in Water: Evidence That This Model Reaction Probes Basicity in Addition to Acidity

Insaf Abdouli , Frederic Dappozze, Marion Eternot, Chantal Guillard  and Nadine Essayem \* 

Institut de Recherches sur la Catalyse et l'Environnement de Lyon, UMR 5256, CNRS, Université Claude Bernard Lyon 1, IRCELYON, F-69626 Villeurbanne, France

\* Correspondence: nadine.essayem@ircelyon.univ-lyon1.fr

**Abstract:** In this paper, evidence is provided that the model reaction of aqueous dihydroxyacetone (DHA) conversion is as sensitive to the TiO<sub>2</sub> catalysts' basicity as to their acidity. Two parallel pathways transformed DHA: while the pathway catalyzed by Lewis acid sites gave pyruvaldehyde (PA) and lactic acid (LA), the base-catalyzed route afforded fructose. This is demonstrated on a series of six commercial TiO<sub>2</sub> samples and further confirmed by using two reference catalysts: niobic acid (NbOH), an acid catalyst, and a hydrotalcite (MgAlO), a basic catalyst. The original acid-base properties of the six commercial TiO<sub>2</sub> with variable structure and texture were investigated first by conventional methods in gas phase (FTIR or microcalorimetry of pyridine, NH<sub>3</sub> and CO<sub>2</sub> adsorption). A linear relationship between the initial rates of DHA condensation into hexoses and the total basic sites densities is highlighted accounting for the water tolerance of the TiO<sub>2</sub> basic sites whatever their strength. Rutile TiO<sub>2</sub> samples were the most basic ones. Besides, only the strongest TiO<sub>2</sub> Lewis acid sites were shown to be water tolerant and efficient for PA and LA formation.



**Citation:** Abdouli, I.; Dappozze, F.; Eternot, M.; Guillard, C.; Essayem, N. TiO<sub>2</sub> Catalyzed Dihydroxyacetone (DHA) Conversion in Water: Evidence That This Model Reaction Probes Basicity in Addition to Acidity. *Molecules* **2022**, *27*, 8172. <https://doi.org/10.3390/molecules27238172>

Academic Editor: Lu Liu

Received: 29 October 2022

Accepted: 21 November 2022

Published: 24 November 2022

**Publisher's Note:** MDPI stays neutral with regard to jurisdictional claims in published maps and institutional affiliations.



**Copyright:** © 2022 by the authors. Licensee MDPI, Basel, Switzerland. This article is an open access article distributed under the terms and conditions of the Creative Commons Attribution (CC BY) license (<https://creativecommons.org/licenses/by/4.0/>).

**Keywords:** titanium dioxide; dihydroxyacetone; CO<sub>2</sub> and NH<sub>3</sub> microcalorimetry; FTIR of pyridine adsorption; acidity; basicity

## 1. Introduction

The replacement of petroleum products by biomass-derived ones has been attracting growing attention in recent years. In this regard, the valorization of biomass and its derivatives into value-added products has been largely studied by means of different processes, especially hydrothermal ones. For these processes, homogeneous and heterogeneous acid-base catalysts were used to catalyze specific reactions steps such as hydrolysis, retro-aldolization, dehydration, etc. However, in hydrothermal conditions, solid acids and bases may be inhibited by water.

Different physicochemical methods are now well established to characterize the original acid-base properties of heterogeneous catalysts. Most of them are performed in the gas phase such as temperature-programmed desorption (TPD) of probe molecules [1–4]; adsorption of probe molecules monitored by microcalorimetry [1,3–5] or infrared spectroscopy (FTIR) [3,4,6], etc. Nevertheless, these techniques characterize heterogeneous catalysts in gas phase, conditions completely different from the hydrothermal medium where acid or basic sites are very often inhibited by water [7,8].

Besides, the use of model reactions is an effective method since they are conducted under conditions as similar as possible to the reactional ones. Model reactions, whose mechanisms are well known, were largely applied in the gas phase such as light alkanes or alkenes isomerization or alcohol dehydration or dehydrogenation [9–12]. Each pathway is specifically catalyzed by acid and/or basic sites. The reactions rates, the products distribution and the mechanism involved may give insight on the nature of the active sites and/or on their density or strength. In the liquid phase, the use of model reactions is less



we measured the original acidity and basicity of six selected commercial TiO<sub>2</sub> samples using well-established gas phase methods: namely, pyridine, NH<sub>3</sub> and CO<sub>2</sub> adsorption monitored by FTIR and microcalorimetry to get reliable data on the nature, density and strength of the original acidity and basicity of each TiO<sub>2</sub> samples in the absence of moisture.

In this work, we use the model reaction of DHA conversion in the aqueous phase to probe the catalyst's Bronsted/Lewis acidity, while demonstrating that this reaction can also probe the basic properties leading to DHA condensation into hexoses. This conclusion was supported by the studies of different commercial TiO<sub>2</sub> samples with variable acid-base properties as established by the usual gas phase methods and by the study of reference acid and base catalysts, i.e., NbOH and MgAlO

## 2. Results and Discussion

### 2.1. Catalysts Characterization

The XRD patterns of the six commercial TiO<sub>2</sub> catalysts are shown in Figure 1. It is confirmed that P25 and P90 are mixtures of anatase and rutile crystalline phases, UV100 and HPX-200/v2 are pure anatase and Rut160 and HPX-400C are pure rutile. From XRD measurements, the average size of TiO<sub>2</sub> crystallites was found to be around 8 nm for UV100 and Rut160, ~12 nm for P90 and HPX-200/v2, 16 nm for HPX-400C and around 20 nm for P25 (Table 1). The crystallite size of UV100 and P25 were in agreement with those determined by Arana et al. [32].

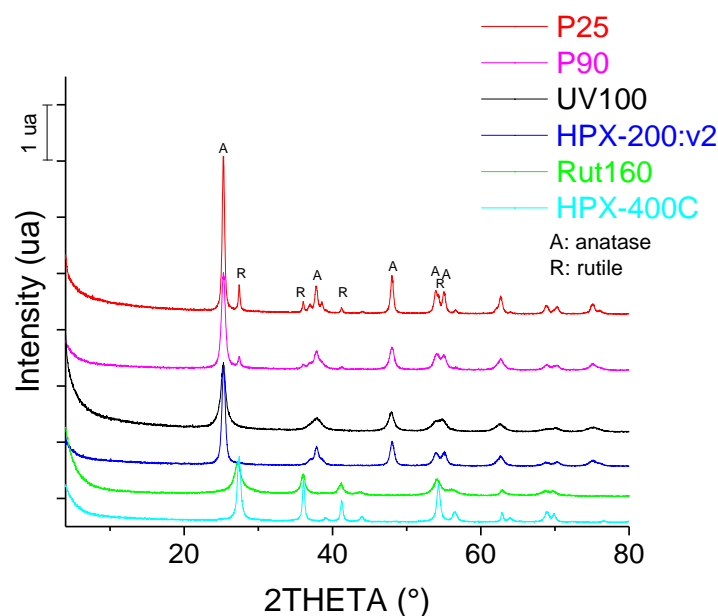


Figure 1. Diffractogram of commercial TiO<sub>2</sub> samples.

Table 1. Textural features and particle sizes of commercial TiO<sub>2</sub> samples.

Catalysts	S <sub>BET</sub> <sup>1</sup> (m <sup>2</sup> .g <sup>-1</sup> )	Mesopores Size <sup>2</sup>	S Micropore <sup>3</sup> (m <sup>2</sup> .g <sup>-1</sup> )	Crystallites Size <sup>4</sup> (nm)
P25 (80% anatase/20% rutile)	55	>4 nm	-	18.1
P90 (92% anatase/8% rutile)	115	>5 nm	-	11.6
UV100	300	>3 nm	194	7.5
HPX-200/v2	96	>4 nm	-	13.1
Rut160	175	>4 nm	82	8.5
HPX-400C	85	>5 nm	-	16.4

<sup>1</sup> Pretreatment: 2 h at 300 °C under vacuum (heating rate: 5 °C.mn<sup>-1</sup>), <sup>2</sup> BJH, <sup>3</sup> t-plot, <sup>4</sup> from XRD patterns.

The BET surface areas are roughly related to the size of the TiO<sub>2</sub> crystallites, which indicates that they are mainly developed by the external surfaces of the particles.

The isotherms shown in Figure 2 present the same feature, the presence of a hysteresis loop at high relative pressure, linked with the presence of large mesopores, above 3–5 nm. UV100 and Rut160 present also micropores as indicated by the significant N<sub>2</sub> adsorption at very low relative pressure. As shown in Table 1, the highest BET surface areas were observed for UV100 (300 m<sup>2</sup>.g<sup>-1</sup>) and Rut160 (175 m<sup>2</sup>.g<sup>-1</sup>), probably due to their smallest crystallites and the presence of micropores. The P25 showed the lowest surface area (55 m<sup>2</sup>.g<sup>-1</sup>), whereas the rest of the samples, i.e., P90 (mixture of anatase and rutile), HPX-200/v2 (anatase) and HPX-400C (rutile), exhibited almost similar surface areas close to 100 m<sup>2</sup>.g<sup>-1</sup>.

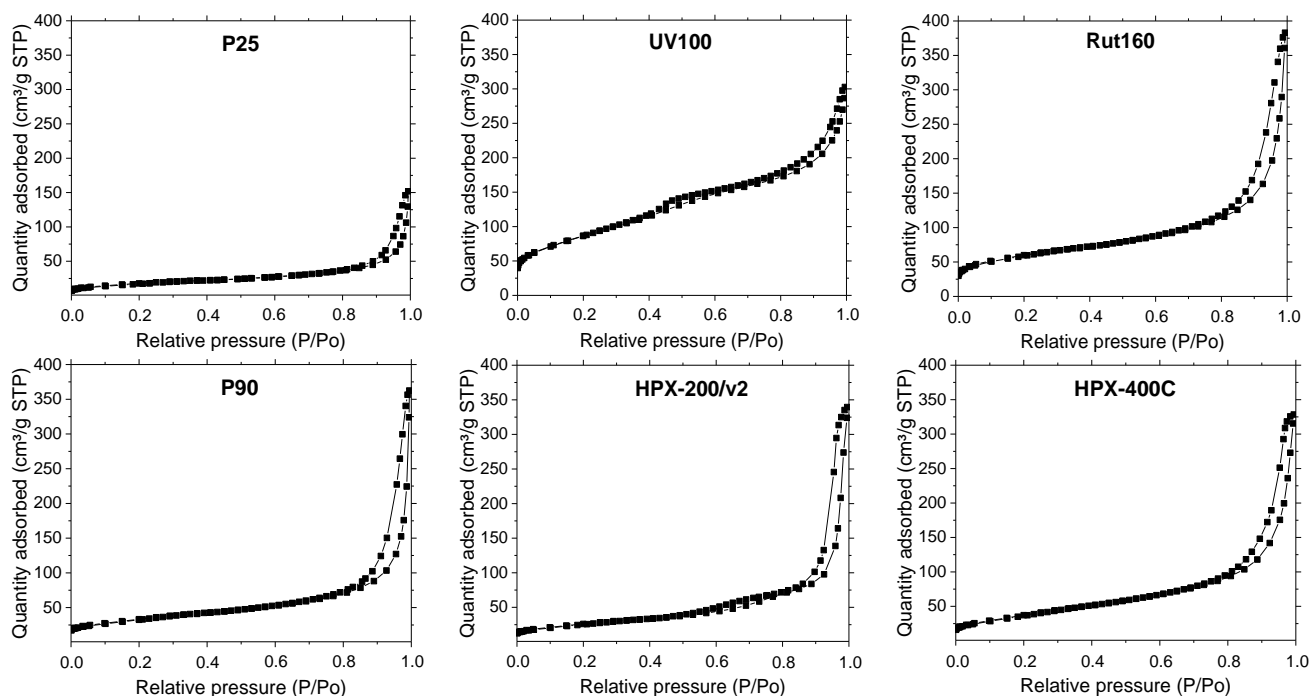


**Figure 2.** N<sub>2</sub> adsorption/desorption isotherm of the commercial TiO<sub>2</sub> samples. Catalyst pretreatment: 300 °C for 2 h under vacuum (heating rate: 5 °C.mn<sup>-1</sup>).

## 2.2. Catalysts' Acidity

The catalysts' acidity was first studied by pyridine adsorption followed by FTIR to identify the nature of the acid sites, Lewis vs. Brønsted. The different FTIR spectra obtained after pyridine adsorption on TiO<sub>2</sub> dehydrated at 150 °C, then vacuum treated at ambient temperature and 150 °C, are shown in Figure 3. All the catalysts exhibited bands at 1445 and 1610 cm<sup>-1</sup> that correspond to the vibrations characteristic of pyridine coordinated to the catalysts' Lewis acid sites. The spectra also show a band at 1490 cm<sup>-1</sup> common to a vibration mode of pyridine coordinated to the catalysts' Lewis acid sites and to pyridinium ions. The band observed at 1575 cm<sup>-1</sup> was previously ascribed to a vibration of pyridine linked by hydrogen bonds to the catalysts' surface [35]. However, no significant peak at 1545 cm<sup>-1</sup> nor at 1640 cm<sup>-1</sup>, corresponding to the vibrations characteristic of the pyridinium ions, formed in the presence of Brønsted acid sites, are clearly observed. Over Rut160 and P25, if present, this vibration is hardly detected from the baseline. Thus, from our FTIR study of pyridine adsorption on the TiO<sub>2</sub> samples dehydrated at 150 °C, one can conclude that all the six TiO<sub>2</sub> samples have only Lewis acid sites in agreement with previous investigations [24,29]. Our study does not demonstrate the presence of Brønsted acidity on these anatase and/or rutile TiO<sub>2</sub> samples, in contrast to others [32].

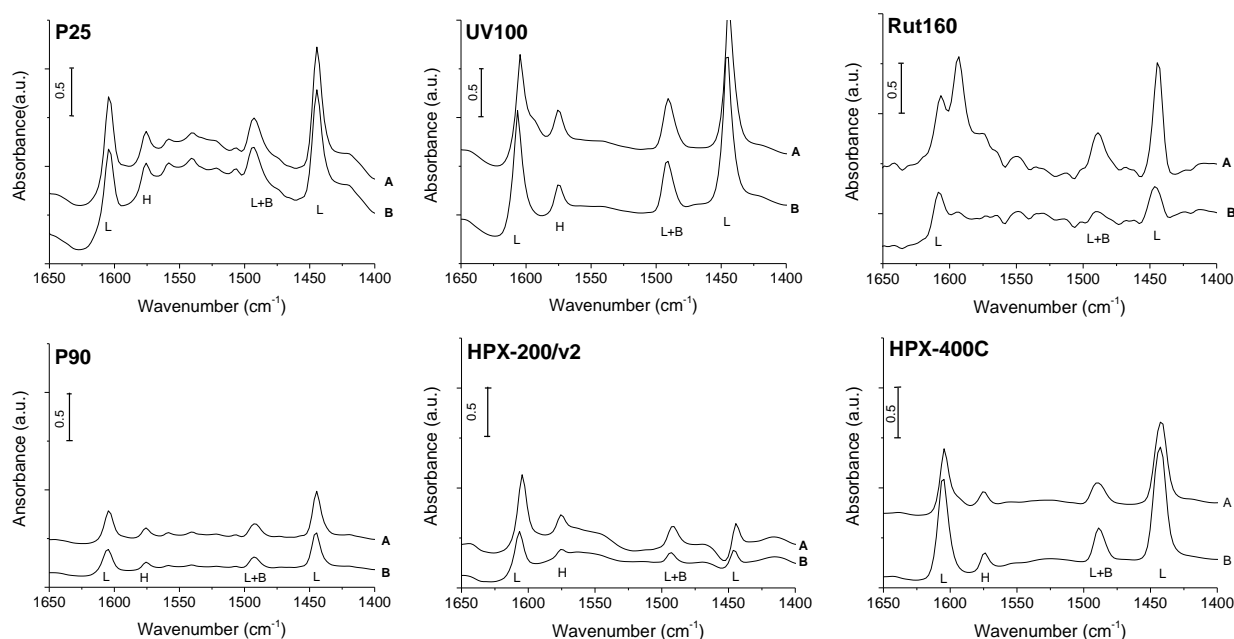


**Figure 3.** Infrared spectra of pyridine adsorption on P25, P90, UV100, HPX-200/v2, Rut160 and HPX-400C: (A) spectra of catalysts saturated with pyridine vapor at ambient temperature, then desorption of pyridine for 1 h at ambient temperature; (B) spectra after pyridine desorption at 150 °C for 1 h (L: characteristic vibration of Lewis acid sites, B: characteristic vibration of Brønsted acid sites, L + B: vibration common to Lewis and Brønsted acid sites, H: vibration of pyridine linked by hydrogen bonds). Conditions: Prior to pyridine adsorption, TiO<sub>2</sub> self-supported pellets were vacuum treated for 1 h at 150 °C (reference spectra), normalized spectra to 100 mg.

The study of the catalysts' acidity was then completed by NH<sub>3</sub> adsorption monitored by microcalorimetry coupled to the NH<sub>3</sub> isotherm measurements: a precise and reliable technique to determine the total number of acid sites and their acid strength distribution. As determined by the adsorption of pyridine followed by FTIR, all the catalysts have only Lewis acid sites; thus, the adsorption of NH<sub>3</sub> monitored by microcalorimetry measures the amount and the density of the Lewis acid sites.

The isotherms of NH<sub>3</sub> adsorption on all the samples dehydrated at 150 °C are compared in Figure 4a and the corresponding calorimetric curves are displayed in Figure 4b. The pure anatase TiO<sub>2</sub>, UV100, which also exhibits the highest BET surface area of 300 m<sup>2</sup>.g<sup>-1</sup>, has more than twice the acid sites (~900 μmol.g<sup>-1</sup>) in comparison to other materials. On the other hand, the P25, which is made of a mixture of anatase and rutile phases with the lowest BET surface area, has the lowest amount of the acid sites, ~200 μmol.g<sup>-1</sup>. Total acid sites amounting to between 240 and 410 μmol.g<sup>-1</sup> are measured on all other TiO<sub>2</sub> samples which also present intermediate BET surface areas. Since the samples have quite different specific surface areas, the calorimetric curves are compared as a function of the acid site density, expressed in μmol NH<sub>3</sub> per square meter (Figure 4b). The calorimetric curves of all the catalysts except Rut160 and HPX-400C show quite an equivalent pseudo plateau which indicated the presence of many acid sites of homogeneous acid strength with heat of NH<sub>3</sub> adsorption between 120 kJ.mol<sup>-1</sup> and 140 kJ.mol<sup>-1</sup> for P25, P90, HPX-200/v2 and UV100. HPX-400C presents a calorimetric curve well above the previous ones, with the presence of stronger acid sites, of homogeneous strength, characterized by a longer pseudo-plateau between 155 and 125 kJ.mol<sup>-1</sup>. In contrast, the calorimetric curve of Rut160 shows a continuous decrease of the heat of ammonia adsorption with the ammonia coverage which indicates the presence of a more heterogenous surface in terms of strength with significant lower acid strength.

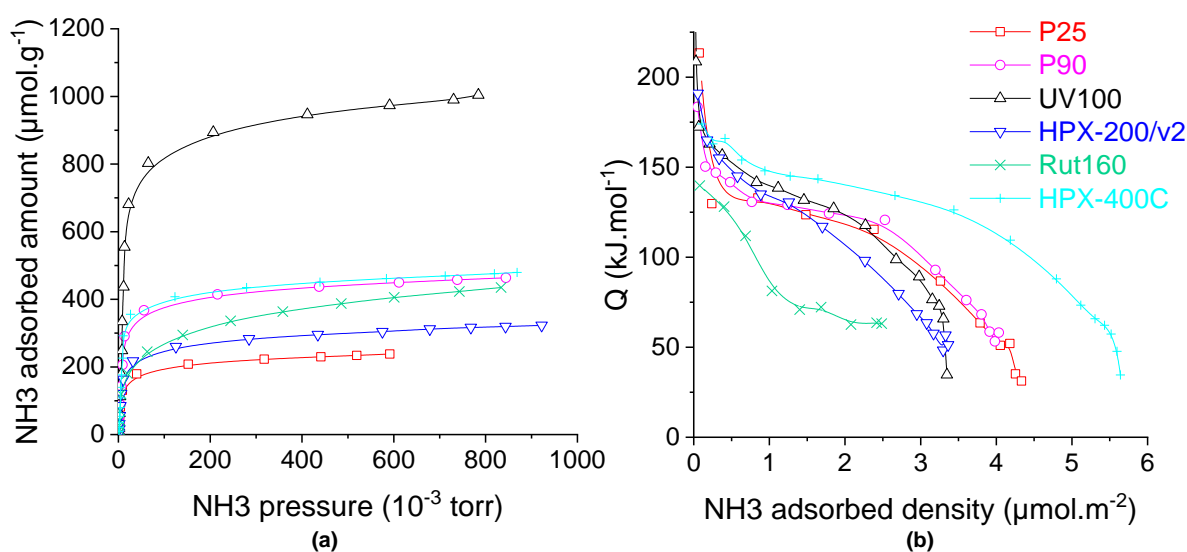


**Figure 4.** Ammonia adsorption on the TiO<sub>2</sub> samples: (a) isotherms and (b) calorimetric curves. Conditions: TiO<sub>2</sub> samples pre-treated at 150 °C under secondary vacuum for 5 h, NH<sub>3</sub> adsorption performed at 80 °C.

Except Rut160, all the TiO<sub>2</sub> samples present few strong acid sites with heat of ammonia adsorption higher than 150 kJ.mol<sup>-1</sup>. Thus, to tentatively understand the effect of catalysts' crystalline phase and/or the crystallites' size on the TiO<sub>2</sub> acidity, the acid sites densities (acid sites amount divided by the catalyst's surface area) are compared in Table 2. As shown in Table 2, catalysts containing only anatase (UV100 and HPX-200/v2) or mainly anatase phase (80% for P25 and 92% for P90) have acid sites densities around 3 μmol.m<sup>-2</sup> with close acid strength distribution. This would indicate that the Lewis acidity of anatase TiO<sub>2</sub> would not be sensitive to the structure (crystallite size). On the contrary, one can observe quite different acid site density on pure rutile TiO<sub>2</sub>: around 1.4 μmol.m<sup>-2</sup> and 5 μmol.m<sup>-2</sup> for Rut160 and HPX-400C, respectively. Since HPX-400C with crystallites' size around 16 nm is more acidic than Rut160 with smaller particles (8.5 nm), one could suggest that the acidity of rutile TiO<sub>2</sub> would be structure sensitive and the Ti<sup>4+</sup> exposed on the faces of the larger crystallites of the rutile TiO<sub>2</sub> HPX-400C would make it more acidic than the rutile TiO<sub>2</sub> Rut160.

**Table 2.** Catalysts' acid/basic sites amounts and densities.

Catalyst	Acid Sites Amount (μmol.g <sup>-1</sup> )	Acid Sites Density (μmol.m <sup>-2</sup> )	Basic Sites Amount (μmol.g <sup>-1</sup> )	Basic Sites Density (μmol.m <sup>-2</sup> )	Acid/Base Sites Ratio
P25	200	3.6	10	0.18	20
P90	400	3.5	15	0.13	27
UV100	900	3	120	0.4	7.5
HPX-200/v2	275	2.9	20	0.2	13.7
Rut160	240	1.4	40	0.23	6
HPX-400C	410	4.8	85	1	4.8

Conditions: TiO<sub>2</sub> samples pretreated at 150 °C under secondary vacuum for 5 h, NH<sub>3</sub> adsorption performed at 80 °C, CO<sub>2</sub> adsorption performed at 30 °C.

### 2.3. Catalysts Basicity

The catalysts' basicity was studied in the gas phase by carbon dioxide adsorption monitored by microcalorimetry. The CO<sub>2</sub> adsorption isotherms (Figure 5a) show that anatase UV100, which has the highest BET surface area (300 m<sup>2</sup>.g<sup>-1</sup>), has the highest amount of basic sites (120 μmol.g<sup>-1</sup>), then the rutile catalysts (HPX-400C and Rut160) have an intermediate basicity (85 and 40 μmol.g<sup>-1</sup>, respectively) not correlated with their surface

areas (85 vs. 175  $\text{m}^2\cdot\text{g}^{-1}$ ). Anatase HPX-200/v2 and anatase/rutile catalysts (P25 and P90) had the lowest basic sites amounts,  $<25 \mu\text{mol}\cdot\text{g}^{-1}$ . Since the different  $\text{TiO}_2$  samples have different surface areas, the calorimetric curves are also displayed as a function of the basic sites' densities (basic sites amount divided by the catalyst's surface area). HPX-400C (rutile) and UV100 (anatase) showed by far the highest basic sites density with a significant proportion of very weak basic sites in the case of HPX-400C, with  $Q_{\text{diffCO}_2}$  between 40 and 80  $\text{kJ}\cdot\text{mol}^{-1}$ . As shown in Table 2, the other catalysts had lower basic sites densities,  $<0.23 \mu\text{mol}\cdot\text{m}^{-2}$ .

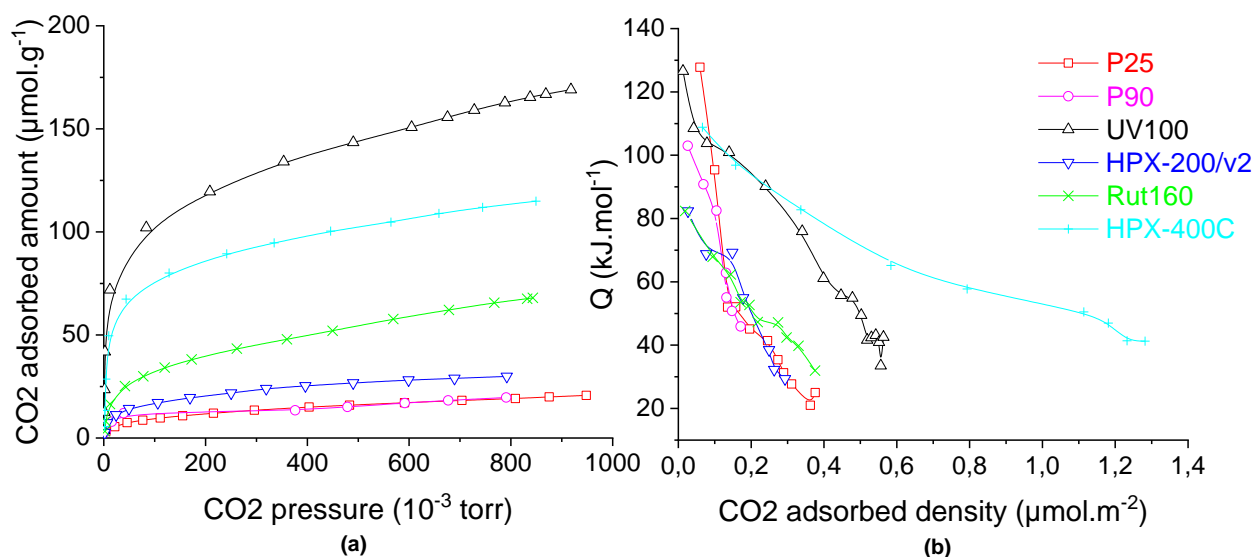


**Figure 5.** Carbon dioxide adsorption on  $\text{TiO}_2$  (a) isotherms and (b) calorimetric curves. Conditions:  $\text{TiO}_2$  samples pre-treated at 150 °C under secondary vacuum for 5 h,  $\text{CO}_2$  adsorption at 30 °C.

The calorimetric curves of the six catalysts (Figure 5b) showed a progressive decrease of  $\text{CO}_2$  adsorption's heat with the  $\text{CO}_2$  coverage which indicates the presence of basic sites with different strength, i.e., quite heterogeneous surfaces in terms of basic strength.

From these values, one can conclude that there is no correlation between either the basic properties and the  $\text{TiO}_2$  structure or the crystallites sizes and specific surface areas.

However, the superficial acid/base balance, reported in Table 2, seems to differentiate the anatase from the rutile phase: the rutile  $\text{TiO}_2$  surfaces appear to exhibit the lowest acid/base balance with a ratio close to 5; while the highest acid/base ratio, between 7.5 and 27, is measured for the pure anatase or the anatase/rutile mixture. In agreement with these remarks, P25, which contains 20% of the rutile phase, presents a lower acid/base balance than P90, which contains only 8% of the rutile phase.

Note that the surface acid/base balance does not seem to depend on the morphology of the  $\text{TiO}_2$  samples nor to the presence of impurities such as S or Cl traces (Table S1).

#### 2.4. DHA Conversion in Water

As discussed above, the model reaction of DHA conversion in water was investigated in the presence of the six  $\text{TiO}_2$  samples with different original acid base properties as characterized above in the gas phase. Our initial goal was to determine, a priori, their Lewis acid sites water tolerance since it is largely accepted that DHA conversion would proceed via an acid catalyzed cascade transformation producing first pyruvaldehyde and then lactic acid in the presence of water-tolerant Lewis acid catalysts. Scheme 1 represents the largely accepted mechanism of DHA transformation.

Figure 6 shows the DHA conversion as a function of time in the presence of the six  $\text{TiO}_2$  catalysts. Among the most active  $\text{TiO}_2$  samples, pure rutile HPX-400C and Rut160 led to DHA conversions around 90% and 80%, respectively, after 400 min of reaction, and UV100 (pure anatase) converted also ~80% of DHA during the same reaction time. The

anatase/rutile mixture, P25, appears as the less active  $\text{TiO}_2$ , leading to the DHA conversion of ~40% at the reaction end. The other anatase/rutile mixture (P90) is slightly more active, with ~60% DHA conversion after 400 min, similar to HPX-200/v2 (pure anatase  $\text{TiO}_2$ ).

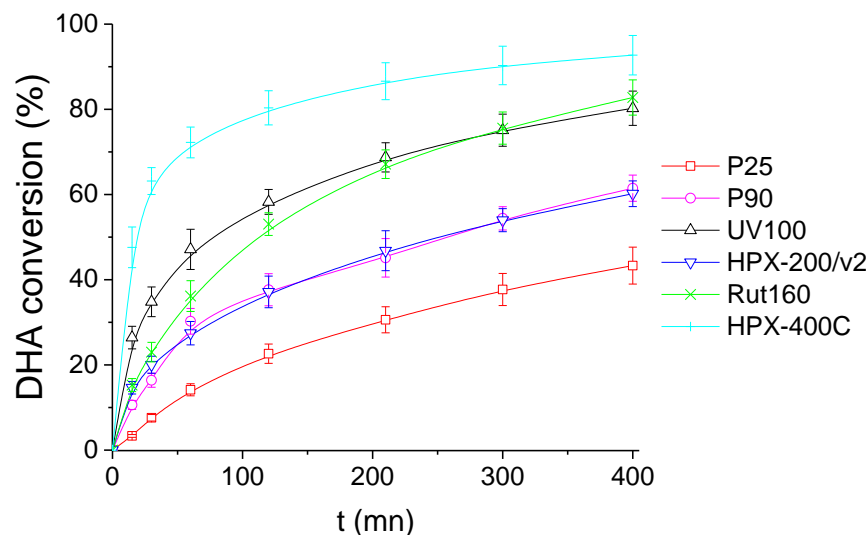


**Figure 6.** DHA conversion with the time course of the reaction in the presence of the six  $\text{TiO}_2$ . Conditions:  $T = 90\text{ }^\circ\text{C}$ ,  $P_{\text{air}} = 1\text{ atm}$ ,  $V_{\text{water}} = 200\text{ mL}$ ,  $(\text{DHA}) = 0.1\text{ mol.L}^{-1}$ ,  $(\text{TiO}_2) = 10\text{ g.L}^{-1}$ .

From the  $\text{TiO}_2$  activity ranking demonstrated in Figure 6 and the acid-base properties summarized in Table 2, the correlation with the basicity is highlighted: the  $\text{TiO}_2$  samples with the lowest acid/basic sites balance, i.e., HPX-400C, Rut160 and UV100, are the most active. Moreover, one can conclude for the absence of any correlation with acidity. Indeed, we searched possible correlations between the initial rate of DHA conversion and the total amount of acid sites ( $\mu\text{mol.g}^{-1}$ ) or the total acid sites densities ( $\mu\text{mol.m}^{-2}$ ) in order to take into account the variability of the samples' surfaces, but no link was observed between the initial rate of DHA conversion and the original acidity of the samples determined in the gas phase (Figures S1 and S2).

We think that these results are of peculiar significance. Indeed, the absence of a correlation between the DHA conversion and the original acidity of the  $\text{TiO}_2$  samples determined in the gas phase might be explained by the variability of the acid sites water tolerance as a function of the  $\text{TiO}_2$  crystallinity or morphologies.

The evolutions of the products' yields with time or with the DHA conversion are presented in Figure 7 and Figure S3, respectively.

In the presence of the most active catalysts, HPX-400C, Rut160 and UV100, the formation of fructose appears as a main initial pathway in the transformation of DHA in addition to PA formation. However, whereas fructose is the main primary product in the presence of Rut160, fructose and PA are two primary products formed in equivalent amount in the presence of HPX-400C, and the formation of PA is initially slightly favoured with respect to fructose in the presence of UV100. In the presence of all the other  $\text{TiO}_2$  (HPX-200/v2, P25 and P90), the initial formation of PA and its further conversion into LA is the main pathway. With the reaction progress over the first three catalysts, the fructose yield declines and we can observe a parallel increase of the glucose formation, explained by the base catalyzed fructose–glucose isomerization. The initial formation of fructose well agreed with the observed link between the  $\text{TiO}_2$  samples' activity and the basicity of their surface. Indeed, fructose, which is C6 sugar, can be formed by aldolic condensation of the trioses DHA and glyceraldehyde, easily formed by DHA isomerization. Note that glyceraldehyde is detected as minor product. Both reactions, aldolic condensation and the aldo-ketose isomerization, responsible for fructose–glucose and DHA–glyceraldehyde isomerization, are base catalyzed steps [36,37]. Accordingly, a linear increase of initial rates of hexoses

formation with the basic sites densities can be drawn (Figure 8). Apparently, the presence of micropores in Rut160 does not interfere with the trioses condensation reaction.

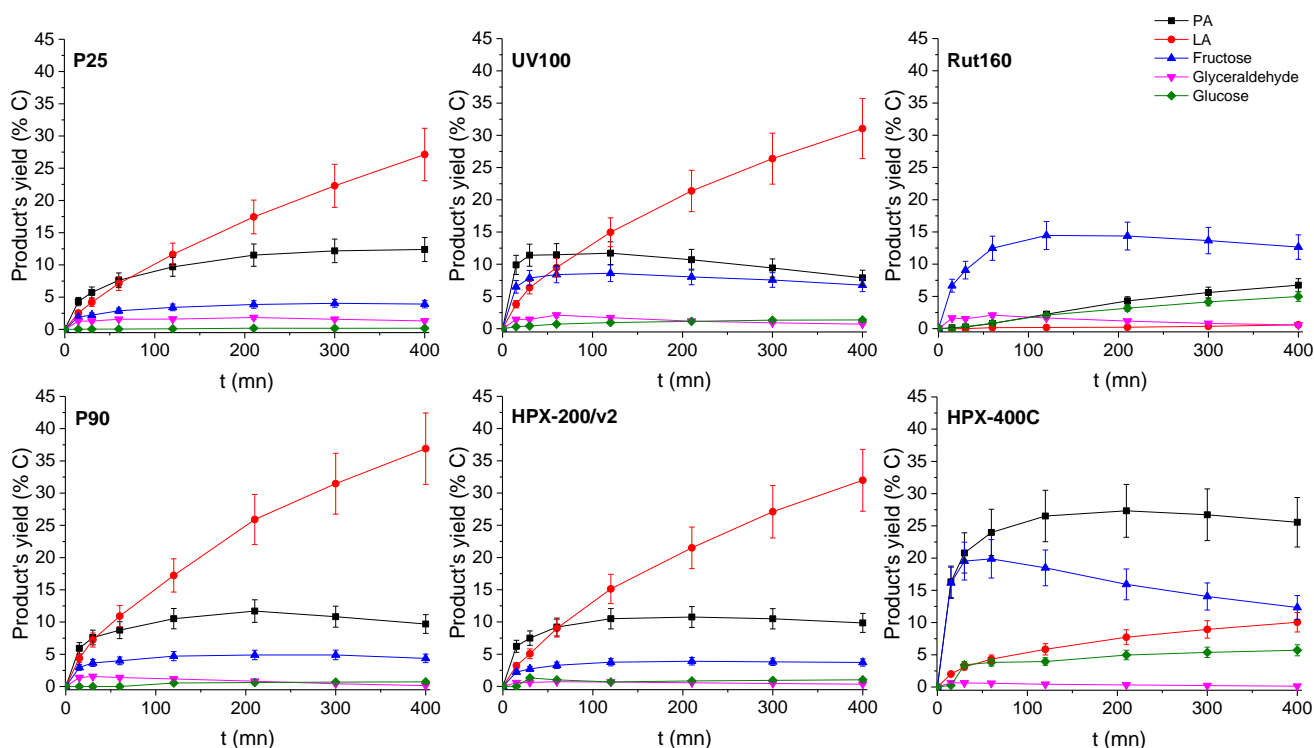


**Figure 7.** Products' yield time course in the presence of the six  $\text{TiO}_2$ s. Conditions:  $T = 90\text{ }^\circ\text{C}$ ,  $P_{\text{air}} = 1\text{ atm}$ ,  $V_{\text{water}} = 200\text{ mL}$ ,  $(\text{DHA}) = 0.1\text{ mol}\cdot\text{L}^{-1}$ ,  $(\text{TiO}_2) = 10\text{ g}\cdot\text{L}^{-1}$ .

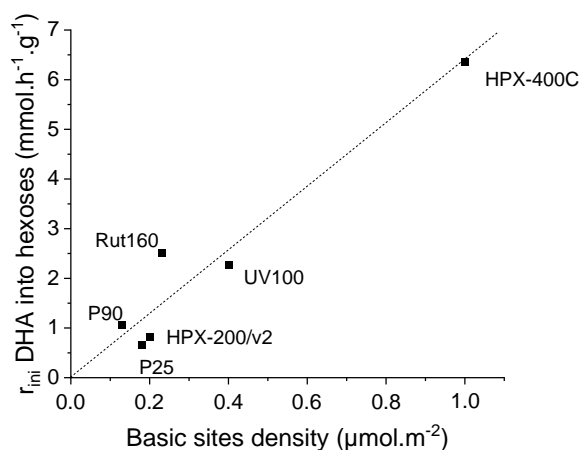


**Figure 8.** Increase of initial rate of hexoses formation as a function of  $\text{TiO}_2$ 's basic sites density.

Besides, the less active materials (P25, P90 and HPX-200/v2) presented activities consistent with the previous art: the initial formation of PA from DHA dehydration, which slows down with the reaction progress while the LA yield continuously increased (Figure 7). This fits well with the generally accepted mechanism which involves, first, an acid catalyzed (Brønsted or Lewis) DHA dehydration, and then, its rehydration into LA in the presence of water-tolerant Lewis acid sites [16,19]. However, it is interesting to note that LA is rapidly formed. At a DHA conversion lower than 10%, the amount of LA is already practically equivalent to that of PA. Such a kinetic profile was already reported over a solely water-tolerant Lewis acid catalyst such as  $\text{Sc}(\text{OTf})_3$  ( $\text{OTf} = \text{triflate}$ ) [38]. Most likely, the two steps, DHA dehydration into PA and its further rehydration into LA, occur solely on the Lewis acid sites of  $\text{TiO}_2$  that have kept efficiency in water. Presumably, this would suggest that

the successive transformation of PA into LA would not be the rate-limiting step when only Lewis acids sites are involved. LA achieved a maximum yield of ~40% over P90 after 6 h corresponding to a selectivity of about 60% at a DHA conversion of 60% against less than 5% for pure rutile. Note that fructose, glucose, and glyceraldehyde were detected over all TiO<sub>2</sub> samples but in low proportions over the less active catalysts. The aldo-ketose isomerization was reported to be catalyzed as well by basic or Lewis acid sites [36,37,39].

Again, we tried to highlight an expected relationship between the initial rates of PA and LA formation and the catalyst acidity. Figure S4 evidences the absence of correlation between the initial rate of PA and LA formation with the total amount of acid sites determined in gas phase expressed per g of catalyst. The initial formation of PA and LA matches more with the total acid site density determined in gas phase and expressed in  $\mu\text{mol m}^{-2}$ : Figure 9 shows a progressive increase of the initial rates of PA and LA formation with the rise of the total acid sites densities.

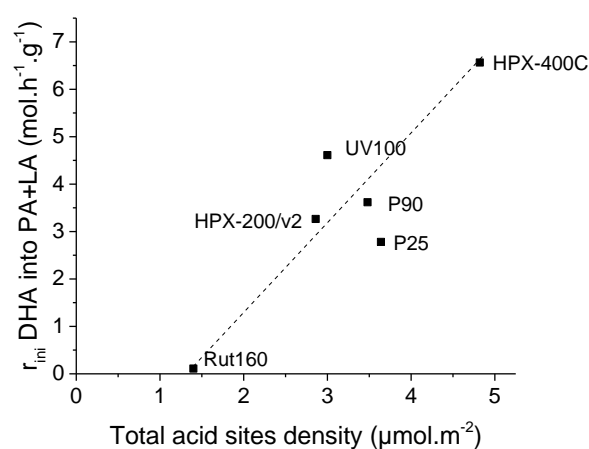


**Figure 9.** Increase of initial rates of pyruvaldehyde and lactic acid formation with TiO<sub>2</sub>'s total acid sites density.

This could have various explanations:

(1) A surface with enhanced proximity between the acid sites could be less inhibited by water adsorption if the DHA adsorption would require several adsorption sites. In other words, a surface with a higher density of Lewis acid sites would favor the competitive adsorption of triose sugars as regards to water, i.e., this type of surface would be more water tolerant when a triose sugar conversion is concerned. This observation is consistent with our previous observation of the improved adsorption of glucose on TiO<sub>2</sub> samples, which have a high density of original Lewis acid sites (determined in the gas phase) [40].

(2) Disagreeing with most of the previous literature, this could also indicate that DHA dehydration–isomerization into pyruvaldehyde and lactic acid could proceed via a bimolecular mechanism with the intermediate formation of dimeric intermediates as suggested in a recent paper [23].

It is also worth noticing that the dashed linear line, which is simply a guide for eyes to highlight the progressive increase of initial PA and LA rates formation, does not pass through the origin point but crosses the X-axis at a value  $\sim 1.5 \mu\text{mol.m}^{-2}$ . Presumably, this could be consistent with the assumption that the water tolerance of the TiO<sub>2</sub> surface as regards to triose sugar adsorption, and then its conversion would require a minimum density of Lewis acid sites or acid strength. In fact, when we plot the initial rate of PA and LA formation against the acid sites' density of the strongest original acid sites, characterized by a heat of ammonia adsorption higher than  $130 \text{ kJ.mol}^{-1}$  as determined by microcalorimetry, the dashed line goes through the origin (Figure 10).

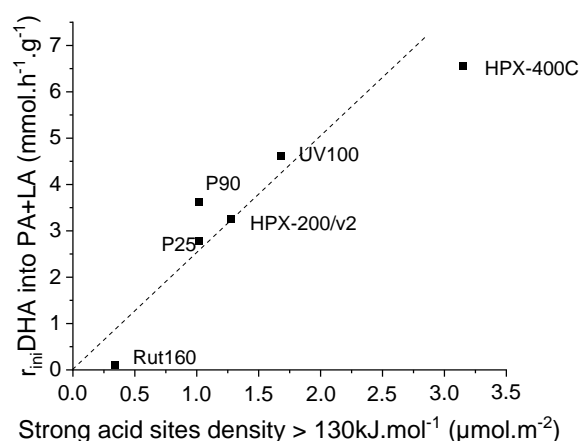


**Figure 10.** Linear increase of the initial rates of pyruvaldehyde and lactic acid formation with  $\text{TiO}_2$ 's original strong acid sites density (sites with heat of ammonia adsorption  $> 130 \text{ kJ.mol}^{-1}$  as determined by calorimetry of ammonia adsorption).

This better correlation would suggest that an additional parameter would intervene for a more efficient adsorption/conversion of triose sugar in water. The higher the strength of the original Lewis acid sites, the more efficient would be the coordination of triose sugar as regards to neutral water. Below these limits, an acid sites density of  $\sim 1.5 \mu\text{mol.m}^{-2}$  and an acid strength of  $130 \text{ kJ.mol}^{-1}$ , the water/triose competitive adsorption would be favorable to water adsorption and the  $\text{TiO}_2$  surface would appear as less water tolerant.

At last, LA yields as a function of DHA conversion are illustrated in Figure 11. It may be seen that, at a given DHA conversion, LA yield was the highest for P25, intermediate for the other anatase  $\text{TiO}_2$  catalysts (pure or mixtures) and almost nil for rutile  $\text{TiO}_2$  (Rut160 and HPX-400C).

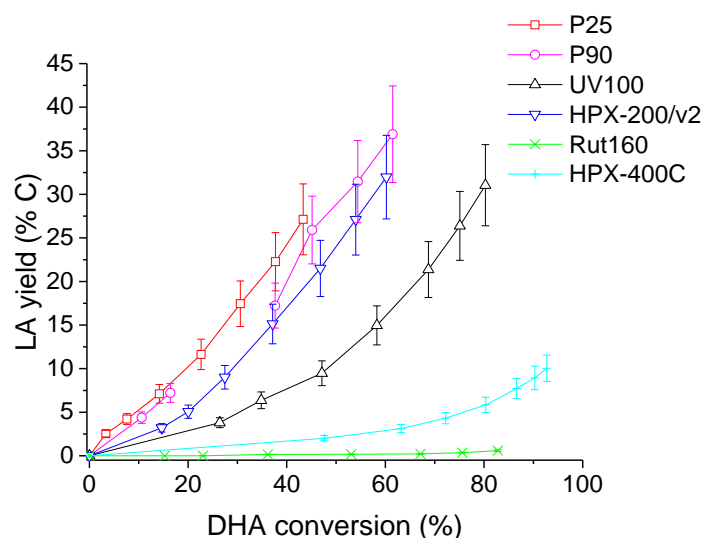


**Figure 11.** Evolution of lactic acid (LA) yield with DHA conversion in the presence of the six  $\text{TiO}_2$ . Conditions:  $T = 90 \text{ }^\circ\text{C}$ ,  $P_{\text{air}} = 1 \text{ atm}$ ,  $V_{\text{water}} = 200 \text{ mL}$ ,  $(\text{DHA}) = 0.1 \text{ mol.L}^{-1}$ ,  $(\text{TiO}_2) = 10 \text{ g.L}^{-1}$ .

To confirm the observed acidity/basicity effect on DHA transformation in the presence of the  $\text{TiO}_2$  catalysts, a well-known water-tolerant solid acid (Lewis and Brønsted acid sites), NbOH [38,41] and a basic heterogeneous catalyst, MgLaO [42,43], were used to convert DHA.

NbOH (Figure 12) exhibited an activity close to the most acid  $\text{TiO}_2$  sample (Figure 7) in water, where PA was initially formed from DHA dehydration and then its formation slowed down with the reaction progress while the LA yield increased continuously. NbOH

produced more PA (maximum yield of 55 C%) (Figure 12) than the most acid TiO<sub>2</sub> catalyst (maximum yield around 15 C%) (Figure 7).

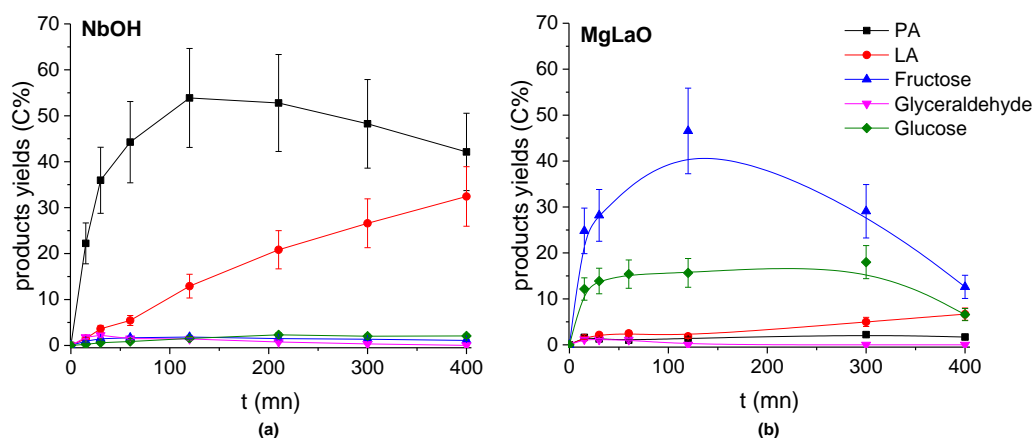


**Figure 12.** Evolution of the Products' yields with the reaction time in the presence of (a) NbOH and (b) MgLaO. Conditions:  $T = 90\text{ }^{\circ}\text{C}$ ,  $P_{\text{air}} = 1\text{ atm}$ ,  $V_{\text{water}} = 200\text{ mL}$ ,  $(\text{DHA}) = 0.1\text{ mol}\cdot\text{L}^{-1}$ ,  $(\text{catalyst}) = 10\text{ g}\cdot\text{L}^{-1}$ .

On the contrary, MgLaO exhibited an activity similar to the most basic TiO<sub>2</sub> (Figure 12) where the main products of DHA conversion were the condensation products: fructose and glucose. PA and LA were formed with very low yields.

Finally, we plotted hexoses selectivities and the sum of PA and LA selectivities at an equivalent DHA conversion level (40%) in Figure 13. The progressive increase of hexoses selectivities against the progressive decrease of PA + LA selectivities is observed. This opposite behavior appears to be roughly linked to the original acid/base balance measured on the TiO<sub>2</sub> samples. The rutile TiO<sub>2</sub>, characterized by the lowest acid/base balance (Table 2), was the most selective for hexoses formation among the TiO<sub>2</sub> samples with a behavior close to that of the reference basic catalyst MgLaO. On the other hand, P25 with the highest acid/base balance was the most selective for PA and LA formation close to the selectivity observed over NbOH, the reference acid catalyst.

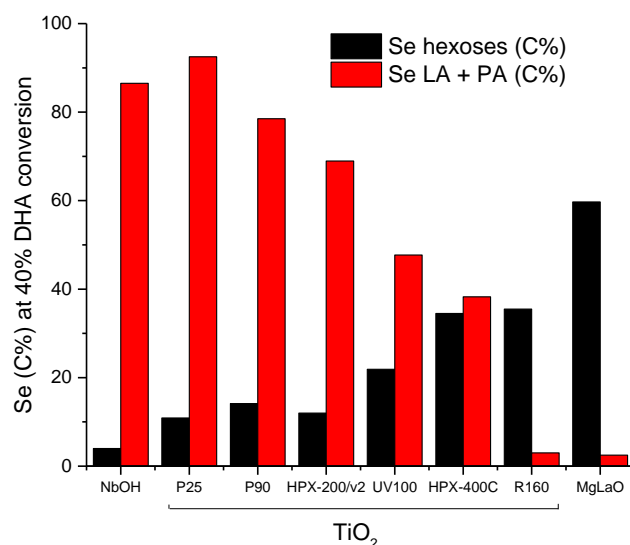
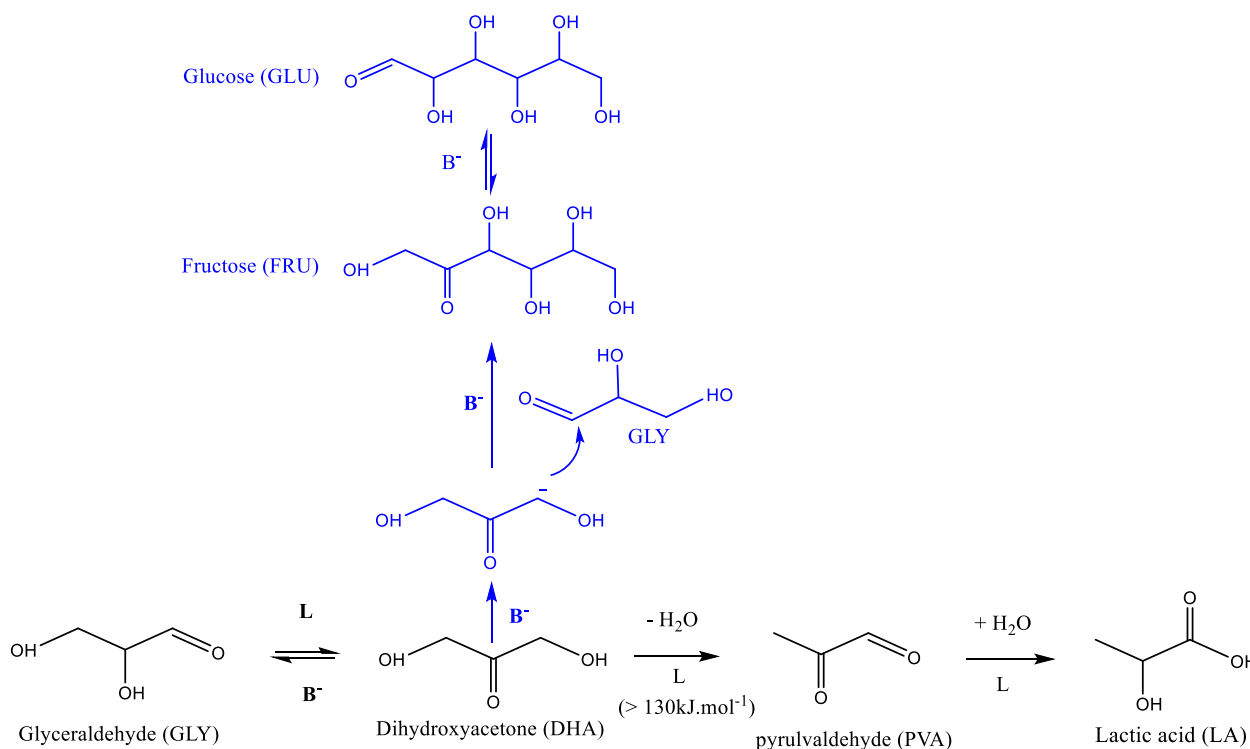


**Figure 13.** Evolutions of hexoses selectivity and Pyruvaldehyde/lactic acid (PA + LA) selectivities at 40% DHA conversion as a function of the TiO<sub>2</sub>'s acid/base balance. Comparison with the reference solid acid, NbOH, and the reference solid base, MgLaO.

So, these results show that DHA conversion can be converted into LA and PA by the catalysts' acid sites and/or to condensation products (fructose, glucose) by the catalysts'

basic sites. This reaction appears as a suitable model reaction to characterize any catalysts' acid and basic sites in water.

To rationalize all the above reported correlations between the original acid or base properties of the  $\text{TiO}_2$  samples and their activities/selectivities for DHA conversion in water, a mechanism is proposed (Scheme 2). This mechanism involves two parallel pathways: one catalyzed by the catalysts' basic sites leading to fructose and glucose and the other one promoted by the strongest Lewis acid sites leading to DHA isomerization into LA. The equilibrium between these two pathways depends on the superficial acid/base balance of the catalyst.



**Scheme 2.** Proposed mechanism which would prevail on bifunctional acid-base catalysts.

### 3. Materials and Methods

#### 3.1. Commercial Titanium Dioxide ( $\text{TiO}_2$ )

Six commercial  $\text{TiO}_2$  with different crystalline phases and different specific surface areas were tested: P25 and P90, which are mixture of anatase and rutile, provided by Evonik, two pure anatase: UV100 from Hombikat and HPX-200/v2 from Cristal and two pure rutile: Rut160 from Nanostructured and Amorphous Materials Incorporation and HPX-400C from Cristal. Rut160 was calcined in a muffle oven at  $400\text{ }^\circ\text{C}$  during 20 h to eliminate organic pollution from its surface. All the other catalysts were used without any treatment. The main impurities of the  $\text{TiO}_2$  samples were summarized in the Table S1.

#### 3.2. X-ray Diffraction (XRD)

The catalysts' crystalline structures and the sizes of their crystallites were analyzed by XRD using a Bruker D8 Advance diffractometer A25 equipped with a copper anode. Powdered samples were analyzed within a  $2\theta$  range of  $4\text{--}80^\circ$  at  $0.02^\circ$  per step and with an acquisition time of 96 s per step. The IRCELYON's XRD Service collected the diffractograms.

#### 3.3. Brunauer–Emmett–Teller Surface Area (SBET) Analysis and Pores' Size Distribution

The catalysts' texture was characterized using nitrogen adsorption/desorption isotherm at  $-196\text{ }^\circ\text{C}$  in a Micromeritics ASAP 2020 device. Before the analysis, the catalysts were degassed at  $300\text{ }^\circ\text{C}$  (heating rate  $5\text{ }^\circ\text{C}\cdot\text{min}^{-1}$ ) during 2 h.

### 3.4. Pyridine Adsorption Monitored by Fourier Transform Infrared Spectroscopy (FTIR)

The acid site types present on the catalysts (Lewis and/or Brønsted) were identified by the adsorption of pyridine monitored by FTIR. FTIR spectra were recorded with a Bruker Vector 22 spectrometer in absorption mode with a resolution of  $2\text{ cm}^{-1}$ . Catalysts powders were pressed into self-supported pellets. The pellets were placed in an IR pyrex cell equipped with  $\text{CaF}_2$  windows and connected to a first vacuum line allowing thermal pretreatment in the absence of pyridine pollution, then the cell was connected to a second piece of vacuum pyrex equipment to perform pyridine adsorption and desorption. All the samples were treated under flowing synthetic air ( $2\text{ L}\cdot\text{h}^{-1}$ ) for one hour at  $150\text{ }^\circ\text{C}$ , then under the secondary vacuum while cooling for one hour. Then, pyridine was adsorbed under saturation vapor pressure at ambient temperature. The pyridine was desorbed for one hour, firstly at ambient temperature, then at  $150\text{ }^\circ\text{C}$  for 1 h (to remove the physisorbed pyridine species on the catalyst). FTIR of pyridine adsorption was only used to discriminate between Lewis and Brønsted acid sites: the 19b vibration mode allows one to discriminate pyridine coordinated to Lewis acid sites ( $1450\text{ cm}^{-1}$ ) from the pyridinium ion ( $1550\text{ cm}^{-1}$ ). In the presence of physisorbed pyridine molecule, this vibration mode is observed at  $1438\text{ cm}^{-1}$  [35].

### 3.5. $\text{NH}_3$ Adsorption Monitored by Microcalorimetry

The number and strength of acid sites of the catalysts were measured by ammonia adsorption at  $80\text{ }^\circ\text{C}$ , monitored by microcalorimetry using a Tian–Calvet calorimeter (MS80 Setaram) coupled with a volumetric equipment for isotherms measurement. This technique allows one to measure the differential heats of adsorption evolved for small and known amounts of ammonia molecules adsorbed on the catalyst surface. This energy depends on the strength of acid sites present on the catalyst surface. The total amount of acid sites is deduced from the isotherms (intersection of the tangent to the Y-axis). Thirty mg of each catalyst were placed in a glass cell and pretreated at  $150\text{ }^\circ\text{C}$  for 5 h under a secondary vacuum (heating rate of  $2\text{ }^\circ\text{C}\cdot\text{min}^{-1}$ ). The cell was then placed in the Tian–Calvet calorimeter stabilized at  $80\text{ }^\circ\text{C}$  for a night and coupled with a volumetric equipment. Finally, successive doses of ammonia were brought into contact with the catalyst while the heats of adsorption were recorded.

### 3.6. $\text{CO}_2$ Adsorption Monitored by Microcalorimetry

The number and strength of the basic sites of the catalysts were measured by the same calorimetric technique but using carbon dioxide as a probe, and the adsorption was done at  $30\text{ }^\circ\text{C}$ . The catalysts (50 mg) were treated exactly as for the acid sites quantification, following the same pretreatment procedure.

The total amount of basic sites is deduced from the isotherms (intersection of the tangent to the Y-axis).

### 3.7. Dihydroxyacetone (DHA) Conversion in Water

The reactions were conducted in a three-neck round bottom flask (250 mL) equipped with a water condenser, a temperature sensor and a rubber septum. At first, water and catalyst ( $10\text{ g}\cdot\text{L}^{-1}$ ) were placed in the flask (total volume of 200 mL) and heated at  $90\text{ }^\circ\text{C}$  in a controlled temperature oil bath and agitated by a magnetic stirrer. When the temperature stabilizes, DHA powder (1,3-dihydroxyacetone dimer, >97%, purchased from Sigma-Aldrich) was added ( $t = 0$ ) and the reactions were conducted during 400 min. The DHA initial concentration was  $0.1\text{ mol}\cdot\text{L}^{-1}$ . Samples were taken with a 1 mL syringe through the septum and analyzed by high-performance liquid chromatography (HPLC): a Shimadzu Prominence system equipped with a refractive index detector (RID) and a COREGEL 107H column maintained at  $40\text{ }^\circ\text{C}$  to quantify the products and the residual substrate (DHA) (Figure S5). The mobile phase was acidified water ( $\text{H}_2\text{SO}_4\text{ }1.7\text{ mM}$ ) with a flow of  $0.6\text{ mL}\cdot\text{min}^{-1}$ .

Two other non TiO<sub>2</sub> catalysts were tested as references for this reaction: a commercial Niobium hydroxide (NbOH) from CBMM, Brazil, and a home-made MgLaO [42].

#### 4. Conclusions

Contrary to all expectations, the most active TiO<sub>2</sub> catalyst for DHA conversion has the most basic surface, as established by calorimetry in the gas phase. The formations of hexoses from DHA on these samples indicates the occurrence of a parallel pathway catalyzed by basic sites. In agreement with the previous literature, lactic acid formation is thought to be linked to the sample's original Lewis acidity.

This was observed on various TiO<sub>2</sub> samples with a variable superficial acid/base balance, and that was confirmed over two reference catalysts: an acid one NbOH and a basic one MgAlO.

Moreover, based on the original acid-base properties of the TiO<sub>2</sub> samples determined in the gas phase and the results obtained studying this model reaction in water, our results suggest that:

- The water tolerance of TiO<sub>2</sub> superficial acidity as regards to triose conversion would require a minimum Lewis acid sites density with enough acid strength ( $Q_{\text{diffNH}_3} > 130 \text{ kJ}\cdot\text{mol}^{-1}$ ).
- The TiO<sub>2</sub> basic sites would be water tolerant whatever their original basic strength.

**Supplementary Materials:** The following supporting information can be downloaded at: <https://www.mdpi.com/article/10.3390/molecules27238172/s1>, Table S1: TiO<sub>2</sub> samples' impurities quantified by X Fluorescence analysis (wt%); Figure S1: Initial rate of DHA conversion as a function of TiO<sub>2</sub>'s acid sites amount determined in the gas phase; Figure S2: Initial rate of DHA conversion as a function of TiO<sub>2</sub>'s acid sites density determined in the gas phase; Figure S3: Evolution of products' yields with DHA conversion in the presence of the six TiO<sub>2</sub>s, NbOH and MgLaO; Figure S4: Initial rate of pyruvaldehyde (PA) and lactic acid (LA) formation as a function of TiO<sub>2</sub>'s acid sites amount determined in the gas phase; Figure S5: HPLC Chromatograph of products after reaction for 400 min catalyzed by P25 (1: glucose, 2: fructose, 3: glyceraldehyde, 4: pyruvaldehyde, 5: lactic acid, 6: dihydroxyacetone).

**Author Contributions:** Investigation, I.A.; validation, I.A., C.G. and N.E.; writing—original draft preparation, I.A.; formal analysis, F.D. and M.E.; writing—review and editing, C.G. and N.E.; funding acquisition, C.G. and N.E.; supervision, C.G. and N.E. All authors have read and agreed to the published version of the manuscript.

**Funding:** This research was funded by the French ANR agency, grant number ANR-17-CE06-0011.

**Data Availability Statement:** The data presented in this study are available on request from the corresponding author.

**Conflicts of Interest:** The authors declare no conflict of interest.

**Sample Availability:** Samples are available on request from the corresponding author.

#### References

1. Damjanović, L.; Auroux, A. Determination of Acid/Base Properties by Temperature Programmed Desorption (TPD) and Adsorption Calorimetry. In *Zeolite Chemistry and Catalysis*; Chester, A.W., Derouane, E.G., Eds.; Springer Netherlands: Dordrecht, The Netherlands, 2009; pp. 107–167, ISBN 978-1-4020-9677-8.
2. Hunger, B.; Hoffmann, J. Temperature-Programmed Desorption (TPD) of Ammonia from H<sup>+</sup>-Exchanged Zeolites with Different Structures. *J. Therm. Anal.* **1988**, *33*, 933–940. [[CrossRef](#)]
3. Che, M.; Vedrine, J.C. *Characterization of Solid Materials and Heterogeneous Catalysts: From Structure to Surface Reactivity*; John Wiley & Sons: Hoboken, NJ, USA, 2012; ISBN 978-3-527-64533-6.
4. Karge, H.G. Concepts and Analysis of Surface Acidity and Basicity. In *Handbook of Heterogeneous Catalysis*; Wiley-VCH: Weinheim, Germany, 2008; Volume 2, pp. 1096–1122, ISBN 978-3-527-61004-4.
5. Auroux, A. Acidity and Basicity: Determination by Adsorption Microcalorimetry. In *Acidity and Basicity*; Molecular Sieves; Springer Berlin Heidelberg: Berlin/Heidelberg, Germany, 2006; Volume 6, pp. 45–152, ISBN 978-3-540-73963-0.
6. Knözinger, H. Infrared Spectroscopy for the Characterization of Surface Acidity and Basicity. In *Handbook of Heterogeneous Catalysis*; American Cancer Society: Atlanta, GA, USA, 2008; pp. 1135–1163, ISBN 978-3-527-61004-4.
7. Hara, M. Heterogeneous Lewis Acid Catalysts Workable in Water. *Bull. Chem. Soc. Jpn.* **2014**, *87*, 931–941. [[CrossRef](#)]

8. Wang, Z.; Fongarland, P.; Lu, G.; Essayem, N. Reconstructed La-, Y-, Ce-Modified MgAl-Hydrotalcite as a Solid Base Catalyst for Aldol Condensation: Investigation of Water Tolerance. *J. Catal.* **2014**, *318*, 108–118. [[CrossRef](#)]
9. Guisnet, M.; Pinard, L. Characterization of Acid-Base Catalysts through Model Reactions. *Catal. Rev.* **2018**, *60*, 337–436. [[CrossRef](#)]
10. Guisnet, M.; Bichon, P.; Gnep, N.S.; Essayem, N. Transformation of Propane, n-Butane and n-Hexane over H<sub>3</sub>PW<sub>12</sub>O<sub>40</sub> and Cesium Salts. Comparison to Sulfated Zirconia and Mordenite Catalysts. *Top. Catal.* **2000**, *11*, 247–254. [[CrossRef](#)]
11. Essayem, N.; Ben Taârit, Y.; Feche, C.; Gayraud, P.Y.; Sapaly, G.; Naccache, C. Comparative Study of N-Pentane Isomerization over Solid Acid Catalysts, Heteropolyacid, Sulfated Zirconia, and Mordenite: Dependence on Hydrogen and Platinum Addition. *J. Catal.* **2003**, *219*, 97–106. [[CrossRef](#)]
12. Drouilly, C.; Krafft, J.-M.; Averseng, F.; Lauron-Pernot, H.; Bazer-Bachi, D.; Chizallet, C.; Lecocq, V.; Costentin, G. Role of Oxygen Vacancies in the Basicity of ZnO: From the Model Methylbutynol Conversion to the Ethanol Transformation Application. *Appl. Catal. Gen.* **2013**, *453*, 121–129. [[CrossRef](#)]
13. Frey, A.M.; Yang, J.; Feche, C.; Essayem, N.; Stellwagen, D.R.; Figueras, F.; de Jong, K.P.; Bitter, J.H. Influence of Base Strength on the Catalytic Performance of Nano-Sized Alkaline Earth Metal Oxides Supported on Carbon Nanofibers. *J. Catal.* **2013**, *305*, 1–6. [[CrossRef](#)]
14. Karaki, M.; Karout, A.; Toufaily, J.; Rataboul, F.; Essayem, N.; Lebeau, B. Synthesis and Characterization of Acidic Ordered Mesoporous Organosilica SBA-15: Application to the Hydrolysis of Cellobiose and Insight into the Stability of the Acidic Functions. *J. Catal.* **2013**, *305*, 204–216. [[CrossRef](#)]
15. Mei, D.; Lercher, J.A. Effects of Local Water Concentrations on Cyclohexanol Dehydration in H-BEA Zeolites. *J. Phys. Chem. C* **2019**, *123*, 25255–25266. [[CrossRef](#)]
16. Jolimaitre, E.; Delcroix, D.; Essayem, N.; Pinel, C.; Besson, M. Dihydroxyacetone Conversion into Lactic Acid in an Aqueous Medium in the Presence of Metal Salts: Influence of the Ionic Thermodynamic Equilibrium on the Reaction Performance. *Catal. Sci. Technol.* **2018**, *8*, 1349–1356. [[CrossRef](#)]
17. Vilcocq, L.; Koerin, R.; Cabiach, A.; Especel, C.; Lacombe, S.; Duprez, D. New Bifunctional Catalytic Systems for Sorbitol Transformation into Biofuels. *Appl. Catal. B Environ.* **2014**, *148–149*, 499–508. [[CrossRef](#)]
18. Taarning, E.; Saravanamurugan, S.; Spangsborg Holm, M.; Xiong, J.; West, R.M.; Christensen, C.H. Zeolite-Catalyzed Isomerization of Triose Sugars. *Chem. Sustain. Energy Mater.* **2009**, *2*, 625–627. [[CrossRef](#)]
19. Hossain, M.A.; Mills, K.N.; Molley, A.M.; Rahaman, M.S.; Talaphol, S.; Lalvani, S.B.; Dong, J.; Sunkara, M.K.; Sathitsuksanoh, N. Catalytic isomerization of dihydroxyacetone to lactic acid by heat treated zeolites. *Appl. Catal. A Gen.* **2021**, *611*, 117979. [[CrossRef](#)]
20. Koito, Y.; Nakajima, K.; Kitano, M.; Hara, M. Efficient Conversion of Pyruvic Aldehyde into Lactic Acid by Lewis Acid Catalyst in Water. *Chem. Lett.* **2013**, *42*, 873–875. [[CrossRef](#)]
21. Albuquerque, E.M.; Borges, L.E.P.; Fraga, M.A.; Sievers, C. Relationship between Acid-Base Properties and the Activity of ZrO<sub>2</sub>-Based Catalysts for the Cannizzaro Reaction of Pyruvaldehyde to Lactic Acid. *ChemCatChem* **2017**, *9*, 2675–2683. [[CrossRef](#)]
22. Santos, K.M.A.; Albuquerque, E.M.; Borges, L.E.P.; Fraga, M.A. Discussing Lewis and Brønsted Acidity on Continuous Pyruvaldehyde Cannizzaro Reaction to Lactic Acid over Solid Catalysts. *Mol. Catal.* **2018**, *458*, 198–205. [[CrossRef](#)]
23. Innocenti, G.; Papadopoulos, E.; Fornasari, G.; Cavani, F.; Medford, A.J.; Sievers, C. Continuous Liquid-Phase Upgrading of Dihydroxyacetone to Lactic Acid over Metal Phosphate Catalysts. *ACS Catal.* **2020**, *10*, 11936–11950. [[CrossRef](#)]
24. Nakajima, K.; Noma, R.; Kitano, M.; Hara, M. Titania as an Early Transition Metal Oxide with a High Density of Lewis Acid Sites Workable in Water. *J. Phys. Chem. C* **2013**, *117*, 16028–16033. [[CrossRef](#)]
25. West, R.M.; Holm, M.S.; Saravanamurugan, S.; Xiong, J.; Beversdorf, Z.; Taarning, E.; Christensen, C.H. Zeolite H-USY for the Production of Lactic Acid and Methyl Lactate from C3-Sugars. *J. Catal.* **2010**, *269*, 122–130. [[CrossRef](#)]
26. Sobus, N.; Krol, M.; Piotrowski, M.; Michorczyk, B.; Czekaj, I.; Kornaus, K.; Trenczek-Zajac, A.; Komarek, S. Conversion of dihydroxyacetone to carboxylic acids on pretreated clinoptilolite modified with iron, copper, and cobalt. *Catal. Commun.* **2022**, *171*, 106509. [[CrossRef](#)]
27. Takagaki, A.; Goto, H.; Kikuchi, R.; Oyama, S.T. Silica-supported chromia-titania catalysts for selective formation of lactic acid from a trise in water. *Appl. Catal. A Gen.* **2019**, *570*, 200–208. [[CrossRef](#)]
28. Komanoya, T.; Suzuki, A.; Nakajima, K.; Kitano, M.; Kamata, K.; Hara, M. A Combined Catalyst of Pt Nanoparticles and TiO<sub>2</sub> with Water-Tolerant Lewis Acid Sites for One-Pot Conversion of Glycerol to Lactic Acid. *ChemCatChem* **2016**, *8*, 1094–1099. [[CrossRef](#)]
29. Kulkarni, A.P.; Muggli, D.S. The Effect of Water on the Acidity of TiO<sub>2</sub> and Sulfated Titania. *Appl. Catal. Gen.* **2006**, *302*, 274–282. [[CrossRef](#)]
30. Silahua-Pavón, A.A.; Espinosa-González, C.G.; Ortiz-Chi, F.; Pacheco-Sosa, J.G.; Pérez-Vidal, H.; Arévalo-Pérez, J.C.; Godavarthi, S.; Torres-Torres, J.G. Production of 5-HMF from Glucose Using TiO<sub>2</sub>-ZrO<sub>2</sub> Catalysts: Effect of the Sol-Gel Synthesis Additive. *Catal. Commun.* **2019**, *129*, 105723. [[CrossRef](#)]
31. Vishwanathan, V.; Roh, H.-S.; Kim, J.-W.; Jun, K.-W. Surface Properties and Catalytic Activity of TiO<sub>2</sub>-ZrO<sub>2</sub> Mixed Oxides in Dehydration of Methanol to Dimethyl Ether. *Catal. Lett.* **2004**, *96*, 23–28. [[CrossRef](#)]
32. Araña, J.; Alonso, A.P.; Rodríguez, J.M.D.; Colón, G.; Navío, J.A.; Peña, J.P. FTIR Study of Photocatalytic Degradation of 2-Propanol in Gas Phase with Different TiO<sub>2</sub> Catalysts. *Appl. Catal. B Environ.* **2009**, *89*, 204–213. [[CrossRef](#)]

33. Busca, G. The Surface Acidity of Solid Oxides and Its Characterization by IR Spectroscopic Methods. An Attempt at Systematization. *Phys. Chem. Chem. Phys.* **1999**, *1*, 723–736. [[CrossRef](#)]
34. Watanabe, M.; Aizawa, Y.; Iida, T.; Aida, T.M.; Levy, C.; Sue, K.; Inomata, H. Glucose Reactions with Acid and Base Catalysts in Hot Compressed Water at 473K. *Carbohydr. Res.* **2005**, *340*, 1925–1930. [[CrossRef](#)]
35. Pichat, P. *Contribution à L'étude de L'adsorption de L'ammoniac et de la Pyridine Sur des Oxydes Isolants à l'aide de la Spectrométrie Infra-Rouge*; Lyon I University: Lyon, France, 1966.
36. Souza, R.O.L.; Fabiano, D.P.; Feche, C.; Rataboul, F.; Cardoso, D.; Essayem, N. Glucose–Fructose Isomerisation Promoted by Basic Hybrid Catalysts. *Catal. Today* **2012**, *195*, 114–119. [[CrossRef](#)]
37. Moreau, C.; Lecomte, J.; Roux, A. Determination of the Basic Strength of Solid Catalysts in Water by Means of a Kinetic Tracer. *Catal. Commun.* **2006**, *7*, 941–944. [[CrossRef](#)]
38. Nakajima, K.; Hirata, J.; Kim, M.; Gupta, N.K.; Murayama, T.; Yoshida, A.; Hiyoshi, N.; Fukuoka, A.; Ueda, W. Facile Formation of Lactic Acid from a Triose Sugar in Water over Niobium Oxide with a Deformed Orthorhombic Phase. *ACS Catal.* **2018**, *8*, 283–290. [[CrossRef](#)]
39. Palai, Y.N.; Shrotri, A.; Asakawa, M.; Fukuoka, A. Silica Supported Sn Catalysts with Tetrahedral Sn Sites for Selective Isomerization of Glucose to Fructose. *Catal. Today* **2021**, *365*, 241–248. [[CrossRef](#)]
40. Abdouli, I.; Eternot, M.; Dappozze, F.; Guillard, C.; Essayem, N. Comparison of Hydrothermal and Photocatalytic Conversion of Glucose with Commercial TiO<sub>2</sub>: Superficial Properties-Activities Relationships. *Catal. Today* **2020**, *367*, 268–277. [[CrossRef](#)]
41. Doiseau, A.C.; Rataboul, F.; Burel, L.; Essayem, N. Synergy Effect between Solid Acid Catalysts and Concentrated Carboxylic Acids Solutions for Efficient Furfural Production from Xylose. *Catal. Today* **2014**, *226*, 176–184. [[CrossRef](#)]
42. Wang, Z.; Fongarland, P.; Lu, G.; Zhan, W.; Essayem, N. Effect of Hydration on the Surface Basicity and Catalytic Activity of Mg-Rare Earth Mixed Oxides for Aldol Condensation. *J. Rare Earths* **2018**, *36*, 359–366. [[CrossRef](#)]
43. Desmartin-Chomel, A.; Hamad, B.; Palomeque, J.; Essayem, N.; Bergeret, G.; Figueras, F. Basic Properties of MgLaO Mixed Oxides as Determined by Microcalorimetry and Kinetics. *Catal. Today* **2010**, *152*, 110–114. [[CrossRef](#)]